RSC Advances

ROYAL SOCIETY OF CHEMISTRY

www.rsc.org/advances

Synthesis and Characterization of Pt Magnetic Nanocatalysts with TiO_2 or CeO_2 layer

Chao Zhang, Yuming Zhou* , Yiwei Zhang*, Qianli Wang, Yuanmei Xu

School of Chemistry and Chemical Engineering, Southeast University, Jiangsu Optoelectronic Functional Materials and Engineering Laboratory, Nanjing 211189, China

Abstract

The Pt magnetic nanocatalysts with TiO_2 or CeO_2 layer have been fabricated successfully. The $mSiO_2/Pt/MO_x/Fe$ hybrids have a CeO_2 or TiO_2 layer synthesized through hydrothermal method and a moveable magnetic Fe core constructed by hydrogen reduction. The obtained nanocapsules were characterized by several techniques, including transmission electron microscopy (TEM), scanning electron microscope (SEM), X-ray diffraction (XRD) and energy dispersion X-ray analysis (EDX). The catalytic evaluation was tested on the reduction of 4-NP to 4-AP monitored by a UV-Vis spectra. The mesoporous SiO_2 shell served as effective barriers to prevent the migration and aggregation of Pt NPs during calcination. Besides, the oxide layers have an apparent co-catalysis effect to improve the catalytic activity. The $mSiO_2/Pt/MO_x/\alpha\text{-}Fe_2O_3$ samples were calcined at different temperatures and the final samples exhibited entirely different catalytic activity. Additionally, a possible mechanism was proposed to explain the results. Furthermore, the synthesized $mSiO_2/Pt/MO_x/Fe$ hybrids could be easily recycled by magnet and the catalytic activity didn't decrease obviously after five runs.

Corresponding author: Yuming Zhou

E-mail: fchem@163.com;

Tel: +86 25 52090617;

Fax: +86 25 52090617.

Key Words: TiO_2, CeO_2, Pt nanocatalyst, Thermal stability

1. Introduction

Noble metals (e.g., Pt, Pd, or Au) NPs have been used to catalyze various chemical reactions successfully such as oxidation of CO, oxidation of alcohols, hydrogenation of acetophenone and propane dehydrogenation, *etc*.[1-5] It is well known that catalytic performances are remarkably affected by the strong interactions between metal and support.[6, 7] Recently, metallic oxides, such as Fe_3O_4, TiO_2, CeO_2, ZnO and ZrO_2[8-12] have been wildly used as supporting materials in the preparation of heterogeneous catalysts. Among them, TiO_2 has attracted strong attention due to its outstanding electrical, photocatalytic and thermal properties.[13-17] For example, Zhang *et al.* [18] reported on the design and the preparation of $mSiO_2/Au/TiO_2/SiO_2$ nanocomposites. In this system, TiO_2 may provide reactive oxygen, resulting in a significantly enhanced activity for CO oxidation. In addition, Brioude and his coworkers[19] have synthesized an eccentric Au@(SiO_2,TiO_2) nanostructure and Zhou *et al.*[16] take the thermal stability and catalytic properties of this distinctive structure into consideration. The calcined Au@(SiO_2,TiO_2) particles showed the highest catalytic activity due to the easy mass transfer, improved thermal stability and increased synergy effect of Au with TiO_2. Lu *et al.*[20] synthesized a triphasic catalytic system (Pt/TiO_2–SiO_2) using a TiO_2 fibrous structure as a strongly interacting oxide support and this composition showed outstanding activity after high-temperature calcinations up to 700°C. Beyond that, CeO_2 have drawn continuous attention also because of their highly enhanced catalytic performance and wide range of applications.[10, 21-24]Wang *et al.*[23] fabricated

the uniform pomegranate-like Pt@CeO_2 multicore@shell nanospheres in a large scale. The asobtained nanospheres exhibited excellent structure stability even being calcined at 600°C for 5 h. Zhou and his coworkers[25] synthesized the uniform Pt/CeO_2 hetero-nanocomposites. Pt precursors were blended evenly in the microemulsion droplets. The synthesized nanocomposites exhibited high thermal stability and improved catalytic activity in the CO oxidation reaction. As mentioned above, both of TiO_2 and CeO_2 showed well synergy effect with Pt NPs and could be used as strongly interacting oxide support. Certainly, other metallic oxides (ZrO_2, ZnO, Cu_2O, SnO_2 *etc.*) have some influence on the catalytic performance of noble catalyst and much scientific effort have been devoted toward the performance comparisons of these oxides.[6, 25-29] However, the key effect of these oxide shells was only limited on the protection of metal NPs ignoring the research of how oxide shells influenced the activity of metal NPs. And few people compare the influence of TiO_2 and CeO_2 on noble catalyst at different temperature specially, especially, when TiO_2 or CeO_2 serve as support layer. Consequently, it is meaningful to implement performance comparisons by synthesized a structure with TiO_2 or CeO_2 layer. Furthermore, We'd better pay attention to the recyclability of the nanocomposites with TiO_2 or CeO_2 layer. In general, α-Fe_2O_3 is a promising material since it has the advantages of low band gap, low cost, and nontoxicity.[30-32]More importantly, α-Fe_2O_3 could be easily transformed to the magnetic Fe by hydrogen reduction at 525°C for 4 h.[33] Synthesized catalysts with Fe component have the specially recycle ability for it could be easily separated by magnet rather than troublesome centrifugation or even distillation. So

these catalysts show wide industrial application prospect. In addition, monodispersed ellipsoidal α-Fe_2O_3 nanoparticles could be synthesized easily through a hydrothermal method.[33] The synthesized ellipsoidal particles have a higher diffusion and catalytic rate than spherical particles for its high aspect ratio.[34] Thus, α-Fe_2O_3 is suitable to be used as a catalyst support material.

Another key factor to keep the high reactivity of noble metal was the remained small metal particles.[35] Generally, much higher activities of the catalysts can be obtained with smaller sizes of noble metal particles.[36] However, during the process of hyperthermal reaction, typically above 300°C, these metal nanoparticles tend to sinter to reduce high surface energies resulting the loss of catalytic activity significantly. Therefore, much research work has been done to keep the metal nanoparticles small size. Recently, many reported works have focused on the stabilization of metal NPs by encapsulating within various oxide layers.[6, 16, 37, 38] It is well known that silica has excellent thermostability and plenty of surface OH groups.[6, 20] In addition, it could be easily synthesized to the porous structure using CTAB as pore-forming agent.[39] And the hydrophilic nature of the mesoporous silica ($mSiO_2$) can induce a wettability control over the catalytic reactions in liquid media resulting the preferential adsorption of hydrophilic liquids into nanoreactor.[40] Therefore, it's reasonable to choose silica as the protection shell to isolate the supported Pt NPs.

From the above, $mSiO_2$ protected small Pt NPs could serve as excelent active-sites. And TiO_2 or CeO_2 layer can enhance the catalytic activity due to the strongly interacting with Pt NPs. In addition, the synthesized ellipsoidal NPs could

show a higher diffusion and catalytic rate because of the high aspect ratio using ellipsoidal α-Fe_2O_3 as hard templates. Furthermore, α-Fe_2O_3 can be transformed to the magnetic Fe and the nanocomposites could be easily separated by magnet. Thus, in this work, we designed the configuration of MO_x/α-Fe_2O_3 deposited with Pt NPs, then covered with a layer of $mSiO_2$. The detailed structure and synthetic procedure was depicted in Fig. 1. In the first step, α-Fe_2O_3 NPs were prepared via a hydrothermal method, and then, coated with a layer of TiO_2 or CeO_2. In the second step, well-dispersed Pt NPs were assembled on the surface of the ellipsoidal NPs via electrostatic interactions. For the third step, a layer of $mSiO_2$ was coated on the surface of the as-synthesized Pt/MO_x/α-Fe_2O_3 NPs. At last, the obtained $mSiO_2$/Pt/MO_x/α-Fe_2O_3 was suffered to calcinations at different temperatures and reduction process with H_2 successively. Thus, the ellipsoidal α-Fe_2O_3 core was transformed to square magnetic Fe core. The resulted samples with different oxide insert layers (TiO_2 or SiO_2) have been evaluated through the reduction of 4-nitrophenol (4-NP) to 4-aminophenol (4-AP) to compare the activities. It was found that the obtained $mSiO_2$/Pt/MO_x/Fe samples exhibited entirely different catalytic performance as the calcination temperature changed from 500°C to 700°C.

2. Experiment

2.1. Materials

potassium tetrachoroplatinate (K_2PtCl_4, ≥96%), (3-aminopropyl)triethoxysilane (APTES), sodium borohydride, trisodium citrate, $Ce(NO_3)_2 \cdot 6H_2O$, hexamethylenetetramine (HMT), cetyltrimethylammoniumbromide (CTAB) and

4-nitrophenol (≥99%) were purchased from Aldrich. $FeCl_3$, KH_2PO_4, tetraethyl orthosilicate(TEOS), tetrabutyl titanate(98%), isopropanol, ethanol, and ammonia solution (25%-28%) were of analytical grade, and all of them were purchased from Sinopharm Chemical Reagent Co., Ltd. Deionized (DI) water was used in all experiment. All chemicals were used as received without further purification.

2.2. Synthesis

Synthesis of ellipsoidal α-Fe_2O_3 NPs.

Monodispersed spindle shaped hematite nanotemplate with controllable aspect ratios were fabricated according to the method described by Chen and co-workers.[33] Typically, 100 mL of aqueous solution containing 2.0×10^{-2} M $FeCl_3$ and 4.0×10^{-4} M KH_2PO_4 were aged at 105°C for 45 h. The resulting precipitate was centrifuged and washed three times with water respectively.

Overcoating of ellipsoidal α-Fe_2O_3 NPs with metals oxides.

(a) Synthesis of TiO_2/α-Fe_2O_3 NPs.

TiO_2 layer was prepared using a method developed by Yin *et al.*[41]The previous α-Fe_2O_3 (0.1 g) particles were dispersed in a mixture of hydroxypropyl cellulose (HPC, 0.2 g), ethanol (40 mL), and deionized water (0.2 mL) under sonication. Then, a stock solution containing 2 mL of tetrabutyl titanate (TBOT) and 20 mL of ethanol was injected into the mixture for at least 10 min. After stirring at 85°C under the refluxing conditions for an additional 100 min, TiO_2/α-Fe_2O_3 colloids were collected by centrifugal separation and washed several times by ethanol. In order to obtain a thicker TiO_2 layer, the coating process was repeated.

(b) Synthesis of CeO_2/α-Fe_2O_3 NPs.

The obtained CeO_2/α-Fe_2O_3 NPs were synthesized according the work of Li *et al.* [42] The previous α-Fe_2O_3 (0.1 g) particles were dispersed in a mixture of ethanol (90 mL) and $Ce(NO_3)_2 \cdot 6H_2O$ (0.05 g), HMT (0.4 g) and deionized water (30 mL) under sonication. Then the solution was stirred at 70°C for 2.5 h. CeO_2/α-Fe_2O_3 NPs were collected by centrifugal separation, and washed several times by ethanol.

Synthesis of Pt/MO_x/α-Fe_2O_3 NPs.

The as-obtained MO_x/α-Fe_2O_3 NPs were added to a solution of isopropanol (100 mL) and APTES (0.5 mL) and heated up to 80°C for 12 h to functionalize with amino groups.[43] The result mixture was collected by centrifugation and washed with isopropanol three times. Then the as-functionalized MO_x/α-Fe_2O_3 NPs were dispersed into a mixture of DI water (100 mL), K_2PtCl_4 (1 mL, 7.11 mg/mL), and trisodium citrate (5 mL, 20 mg/mL) at room temperature (RT). After magnetic stirring for 30 min, fresh sodium borohydride (10 mL, 0.008 mg/mL) was immediately injected to the solution under vigorous stirring. After stirring at RT for 12 h, Pt/MO_x/α-Fe_2O_3 composition was synthesized and isolated by centrifugation. Finally, the collected products were dried at 60°C for 6 h.

Overcoating of Pt/MO_x/α-Fe_2O_3 with mSiO_2

The mSiO_2 layer was constructed via a modified Stöber method using CTAB as the template.[39] In brief, the as-obtained Pt/MO_x/α-Fe_2O_3 NPs were added into a solution containing 60 mL of water, 30 mL of ethanol, 150 mg of CTAB, and 0.55 mL of ammonia solution under mildly stirring for 1 h to form a homogeneous solution. Then

0.2 mL of TEOS was slowly injected into the solution and stirring continually for 4 h. At last, $mSiO_2/Pt/MO_x/\alpha\text{-}Fe_2O_3$ nanoparticles were obtained by centrifugation and washed with ethanol several times.

The preparation of magnetic $mSiO_2/Pt/MO_x/Fe$ nanocapsules

To transform the as-synthesized $mSiO_2/Pt/MO_x/\alpha\text{-}Fe_2O_3$ composition into magnetic $mSiO_2/Pt/MO_x/Fe$ nanoparticles, the sample was calcined at 500°C or 700°C in air for 4 h respectively. Then, the powder was transferred to a tube furnace with ultrapure hydrogen (99.99%) flow at 500°C for 2 h.

2.3. Characterization

Transmission electron microscopy (TEM) experiments were conducted on a JEM-1230 microscope operated at 100 kV. The samples for the TEM measurements were suspended in ethanol and supported onto a Cu grid. Scanning electron microscope (SEM) was performed on a Hitachi S-3400N scanning electron microscope and energy dispersion X-ray analysis (EDX) were conducted on a JEM-1230 microscope operated at 100 kV. The powder X-ray diffraction (XRD) patterns were recorded on a Bruker D8 Advance Diffractometer (Germany) with Cu Kα radiation (λ=1.5406 Å). UV-vis spectra were recorded on a Shimadzu UV 3600 spectrometer.

2.4. Catalytic evaluation

In this experiment, the reduction of 4-NP by $NaBH_4$ was chosen as a model reaction to study the catalytic properties. The as-prepared $mSiO_2/Pt/CeO_2/Fe$ nanoparticles were tested by comparison with $mSiO_2/Pt/TiO_2/Fe$ samples. In a typical run, 0.03 mL

of 4-NP (0.01 M, aqueous solution) was mixed with 0.5 mL of freshly prepared $NaBH_4$ (0.25 M, aqueous solution), 2 mL H_2O in a quartz cell (3.0 mL) and 0.5 mL of aqueous solution of $mSiO_2/Pt/MO_x/Fe$ nanoparticles (1 mg/mL). The absorption spectra were recorded on a UV-Vis spectrophotometer at a regular interval in the range of 250-800 nm. For the recycling experiment, the catalysts were collected by magnet, washed with deionized water, dried at 70°C and reused in the next cycle.

3. Results and discussion

3.1. Characterization of $mSiO_2/Pt/MO_x/Fe$ nanocapsules

The main experimental procedures and the observations are summarized in Fig. 2. As can be seen, α-Fe_2O_3 nanoparticles with high aspect ratio were successfully synthesized under hydrothermal conditions (Fig. 2a and Fig. S3). And the SEM image of α-Fe_2O_3 (Fig. 2b) matches with Fig. 2a. Both of the α-Fe_2O_3 nanoparticles have an elliptical morphology (>400 nm in length) and a high aspect ratio (Fig. 2a and Fig. 2b). TEM of $Pt/CeO_2/\alpha$-Fe_2O_3 NPs (Fig. 2c) shows that CeO_2 layer has a rough morphology (*ca.* 10 nm in thickness) due to the larger nanocrystallites of CeO_2 probably. And the morphology of CeO_2/α-Fe_2O_3 NPs is rough as well (Fig. S1a). Furthermore, since CeO_2 particles have a grey black appearance similar to Pt NPs, the loaded Pt NPs can't be observed apparently. By contrast, the barely visible dark dots could be discovered on the ellipsoidal nanocapsules in Fig. 2d, which may suggest the small size of loaded Pt NPs. At a higher magnification, the homogeneous distribution of Pt NPs (*ca.* 2.55 nm in diameter) can be clearly seen from Fig. S1b. In addition, as observed, a uniform mesoporous silica layer (*ca.* 30 nm in thickness) was deposited

onto the surface of $Pt/MO_x/\alpha\text{-}Fe_2O_3$ by the hydrolysis of TEOS with CTAB as pore-forming agent (Fig. 2e and Fig. 2f). The as-synthesized $mSiO_2/Pt/MO_x/\alpha\text{-}Fe_2O_3$ nanocapsules showed a typical core-shell structure with a smooth surface. The amplifying TEM image of Fig. S1c and Fig. S1d reveal that SiO_2 layer consist of dense mesoporous (*ca.* 2~3 nm in diameter)[39], and the ordered mesoporous could served as channels for the diffusion of reactants.

Fig. 3 shows the UV−visible spectra of all the samples. The curve of Fig. 3a shows a typical spectrum of TiO_2 with a fundamental absorption sharp edge around 320 nm[44], suggesting the successive overcoating of TiO_2 layer. Additionally, as shown in Fig. 3b, an absorption band at about 270 nm arises from the excitation of surface plasmon mode of the Pt NPs[45] indicating the existence of Pt NPs. Furthermore, the selected area electron diffraction (SAED) pattern shown in Fig. S4 confirms the successful synthesis of TiO_2 layer and Pt NPs as well. For comparison, when the $Pt/TiO_2/\alpha\text{-}Fe_2O_3$ nanoparticles are coated with a mesoporous silica shell, the thick shell would mask the optical property of Pt NPs. As a result, this adsorption becomes weaker apparently (Fig. 2c). Furthermore, the $\alpha\text{-}Fe_2O_3$ nanospindles have a visible absorption band from 400 to 550 nm due to the narrow band gap of $\alpha\text{-}Fe_2O_3$ (~2.2 eV).[46] Consequently, the corresponding band (400 to 550 nm) appeared on each of the curves (Fig. 3).

The SAED pattern shown in Fig. 4b confirms the crystalline nature of the loaded CeO_2 NPs, and the high-resolution TEM image (HRTEM) (Fig. 4a) shows a lattice fringes measured with a spacing of 0.312 nm, corresponding to the (111) atomic plane

of the cubic ceria.[21] Certainly, these facts are consistent with the rough surface of CeO_2/α-Fe_2O_3 nanocapsules (Fig. S1a). More importantly, a dim ring along with the blue dashed arc corresponds to the (111) plane of face centered cubic fcc platinum suggesting the load of Pt NPs. Besides, the week trace may due to the small size and the well dispersion of Pt NPs. From the EDX analysis of Fig. 4c, the synthesized Pt/CeO_2/α-Fe_2O_3 sample with the Pt content is 4.42%. However, the Pt content of Pt/CeO_2/α-Fe_2O_3 sample is 6.66% (Fig. 4d) higher than Pt/CeO_2/α-Fe_2O_3 sample. This may due to the plenty of hydroxy on TiO_2 surface.[47] In order to obtain the monodispersed magnetic nanocapsules, as shown in Fig. 1, the non-magnetic mSiO_2/Pt/MO_x/α-Fe_2O_3 samples were calcined at different temperature firstly and then subjected to a reduction process with ultrapure hydrogen (99.99%) at 500°C for 2 h. The colour of the treated powder changed from red to black and the internal surface of cooling tube furnace appeared few drops. The abundant steam may come from the oxidation-reduction reaction of α-Fe_2O_3 with H_2. So the structure of the nanopowder changed certainly. Just as can be seen from Fig. 4e and Fig. 4f, the spindle Fe_2O_3 core was transformed to magnetic Fe core and a small cavity between the Fe core and mSiO_2/MO_x shell appeared comparing with Fig. 2e and Fig. 2f. Obviously, the ellipsoidal morphology of all the nanoparticles maintained and a typical yolk-shell structure was constructed successfully. Besides, the diameter of Pt NPs (*ca.* 4.52 nm in diameter) increased to a certain degree after high temperature treats (Fig. 4f and Fig. 6c).

The crystal structure and composition of these nanocapsules were characterized

by powder X-ray diffraction (XRD). Both of $mSiO_2/Pt/CeO_2/\alpha\text{-}Fe_2O_3$ and $Pt/TiO_2/\alpha\text{-}Fe_2O_3$ samples displayed the peaks at $2\theta = 24.1^o$, 33.2^o, 35.6^o, 40.9^o, 49.5^o and 54.1^o, corresponding to the (012), (104), (110), (113), (024) and (116) crystal planes of $\alpha\text{-}Fe_2O_3$ respectively. However, in comparison, both of Fig. 5c and Fig. 5d displayed the peaks at $2\theta = 44.7^o$, 65.0^o, and 82.3^o, corresponding to the (110), (200), and (211) planes of Fe, indicating the reduction of the Fe_2O_3 core to Fe mostly. The week peak at $2\theta = 40.9^o$ may be attributed to the reflection from (113) plane of the rare residual $\alpha\text{-}Fe2O_3$. Additionally, the curves of Fig. 5a and Fig. 5c exhibited the peaks at $2\theta = 28.6^o$, 47.5^o and 56.3^o due to the reflection from the (111), (220) and (311) planes of the cubic fluorite CeO_2 suggesting the nanocrystalline property of the CeO_2 layer. Furthermore, Pt peaks of the prepared catalysts cannot be observed may because of the low Pt content, indicating either a high dispersion of Pt NPs or small Pt particle size.[48] Beyond that, the strong diffractions of Fe core might mask the peaks of small Pt NPs, TiO_2 interlayer and $mSiO_2$ layer.[46] Similarly, the absence of the peaks of TiO_2 could be attributed to the small TiO_2 grain size.[49]

3.2. Catalytic reduction of 4-nitrophenol

Having discussed the synthesis and morphology of the platinum catalyst nanostructures, we now evaluated the catalytic properties by employing the reduction of 4-nitrophenol (4-NP) into 4-aminophenol (4-AP) as a model reaction, which was demonstrated to be useful for the analysis of the catalytic activity of noble metal nanocatalyst.[6, 16, 37] To exclude the influence of the concentration of $NaBH_4$ on the reduction rate, an excess amount of $NaBH_4$ was added and the reduction process

could be regarded as a first-order reaction with regard to 4-NP. After the addition of $NaBH_4$, the absorption maximum of 4-NP at 317 nm shifted to 400 nm due to the formation of 4-nitorphenolate ion.[50] Besides, 4-NP was inert to $NaBH_4$ and the reduction would not proceed without catalyst. However, after the addition of the catalyst, the absorption peak at 400 nm gradually dropped with a new peak appearing at 299 nm as shown in Fig. 6 a. And the isobestic point at 313 nm indicates the reaction proceeded without any byproducts. In all catalytic runs, the dosage of every reagent kept constant.

Fig. 6b showed the linear relationships between $\ln(C_o/C_t)$ and reaction time in the reaction catalyzed by different samples (C_t is the ordinate values of the absorption peak at 400 nm), and the plots well matched the first-order reaction kinetics. According to the linear relationship, the reaction rate constant k could be calculated from the slopes of the straight lines. The apparent rate constant (k_{app}) of the as-prepared Ce-700 sample was 0.0819 min^{-1}. However, in sharp contrast, the sample of Ce-500 shows the highest catalytic activity (0.452min^{-1}) in this work which is roughly 5.5 times higher than that of the Ce-700 sample. The fact revealed that calcination temperature played a key role in the reaction rate of $mSiO_2/Pt/CeO_2/Fe$ nanocatalyst. From Fig. 6e, the loaded CeO_2 NPs kept its loose and rough morphology similar to the sample without calcination (Fig. 4e) revealing that the calcination temperature (500°C) had little effect on the structure of the nanocapsules. But, as can been seen from Fig. 6f, the rough CeO_2 NPs were transformed into the spherical particles (*ca.* 10 nm in diameter) with smooth surface. The agglomeration of CeO_2

NPs may due to the high calcination temperature (700°C).[51–]Additionally, few obviously black spots (*ca.* 10 nm in diameter) appeared marked with blue dashed circles. The obviously black spots might be attributed to the sintering of Pt NPs.[6] Besides, it is reasonable to speculate that the element of Pt could be wrapped into the smooth spherical CeO_2 particles and the Pt active sites can't contact with reactants. The sintering of CeO_2 NPs and Pt NPs may lead to the enormous loss of active surface area. Consequently, the catalytic activity of $mSiO_2/Pt/CeO_2/Fe$ reduced significantly. For comparison, the sample with TiO_2 layer showed totally different behaviors. The k_{app} obtained from the slope of the linearly plot of Ti-500 is 0.173 roughly 1.8 times higher than that of Ti-700 (0.0949 min^{-1}) revealing that the samples with TiO_2 layer showed excellent thermal stability. The nanocapsules of $mSiO_2/Pt/TiO_2/Fe$ calcined at different temperature almost had no differents in structure expect for the diameter of Pt NPs. As shown in Fig. 6c and Fig. 6d, the diameter of Pt NPs increased from 4.52 nm to 5.2 nm indicating the well anti-sintering ability. And, of course, the decreased k_{app} of $mSiO_2/Pt/TiO_2/Fe$ could be ascribed to the increased diameter of Pt NPs.

It is well known that k_{app} values are in direct proportion to the content of Pt NPs. Therefore, it is necessary to eliminate the influence of Pt content. As can be seen from Fig. S2e and Fig. S2f, the contents of Pt in Ce-500 and Ti-500 are 4.35% and 7.92% respectively. As a result, the normalized k_{app} (k_{napp}) for Ce-500 is 10.4 min^{-1} almost 4.7 times higher than that of Ti-500 (2.18 min^{-1}). Consequently, CeO_2 layer shows excellent co-catalysis effect compared to TiO_2 layer when the catalyst used in relatively low temperature (for example, below 500°C). Furthermore, Ce-700 and

Ti-700 exhibited the k_{napp} of 1.88 and 1.2 min^{-1} respectively. Ce-700 lost the main reaction activity compared to Ti-700, so it is reasonable that the catalyst with TiO_2 layer could be used in high temperature (for example, above 700°C) reaction preferentially considering the conservation of resources.

To explain the above experimental results, we propose a possible catalytic mechanism illustrated in Fig. 7. It is known that Fermi level alignment occurs whenever a metal and semiconductor are placed in contact, resulting in charge redistribution and the formation of a depletion layer surrounding the metal.[52] If Pt (5.65 eV) had a higher work function than contacted MO_x layer, electrons could leave the MO_x layers into Pt NPs resulting in an electron-enriched region. So the lower work function of MO_x layer, the more intensive electron in the interface region. And CeO_2 (4.64) has a lower work function than TiO_2 (5.18)[53], as a result, Ce-500 showed higher catalytic activity than Ti-500.

Last but not the least, the reusability was an necessary quality for a good catalyst considering the operational cost and wastewater treatment in the industrial process. In the recycling experiments, the catalysts could be easily collected by magnet. Then the nanoparticles was washed with deionized water, dried at 70°C and reused in the next cycle. The results revealed that the $mSiO_2/Pt/MO_x/Fe$ catalysts showed good reusability and the 4-NP conversion didn't decrease obviously even after 5 cycles (Fig. S5). Besides, the TEM images of Fig. S6 and Fig. S7 revealed that the structures of the nanocapsules remained the same after severals cycles. The slightly decrease in activity can be ascribed to the loss of catalyst during washing. Hence, it is believed

that the microsized structures of the $mSiO_2/Pt/MO_x/Fe$ hybrids have an important potential value in practical applications.

4. Conclusion

A synthetic protocol has been developed to construct the $mSiO_2/Pt/MO_x/Fe$ structure. The hybrids have a CeO_2 or TiO_2 co-catalysis layer and a moveable magnetic Fe core. Besides, the outer $mSiO_2$ layer (*ca.* 30 nm in thickness) could increase the ability of resisting thermal sintering. The slightly decreased k_{napp} of $mSiO_2/Pt/TiO_2/Fe$ compared to $mSiO_2/Pt/CeO_2/Fe$ demonstrated the high thermal stabiliby of TiO_2 layer. Furthermore, the excellent performance of Ce-500 and the significantly deceased catalytic activity of Ce-700 revealed that the CeO_2 layer is suit to relatively low temperature (for example, below 500°C) reaction. In addition, the sample of Ce-500 and Ti-500 kept high performance even after five cycles of reusing. Future work will involve the synthesizing of a new structure composite.

Acknowledgments

The authors are grateful to the financial supports of National Natural Science Foundation of China (Grant No. 21376051, 21106017, 21306023 and 51077013), Natural Science Foundation of Jiangsu (Grant No.BK20131288), Fund Project for Transformation of Scientific and Technological Achievements of Jiangsu Province of China (Grant No. BA2011086), Specialized Research Fund for the Doctoral Program of Higher Education of China (Grant No.20100092120047), Key Program for the Scientific Research Guiding Found of Basic Scientific Research Operation Expenditure of Southeast University (Grant No. 3207043101) and Instrumental

Analysis Fund of Southeast University.

References

1. J. C. Bauer, T. J. Toops, Y. Oyola, J. E. Parks, S. Dai and S. H. Overbury, *Catal. Today*, 2014, 231, 15-21.

2. A. Villa, C. E-Chan-Thaw, M. Schiavoni, S. Campisi, D. Wang and L. Prati, *Chinese J. Catal*, 2014, 35, 945-951.

3. H. Paul, S. Basu, S. Bhaduri and G. K. Lahiri, *J. Organomet. Chem*, 2004, 689, 309-316.

4. Y. W. Zhang, Y. M. Zhou, J. J. Shi, S. J. Zhou, Z. W. Zhang, S. C. Zhang and M. P. Guo, *Fuel Process Technol.*, 2013, 111, 94-104.

5. S. Guo and S. Sun, J. Am. Chem. Soc., 2012, 134, 2492-2495.

6. S. Xiang, Y. Zhang, Y. Zhou, Z. Zhang, X. Sheng and Y. Xu, *RSC Adv.*, 2014, 4, 51334-51341.

7. Z. Guo, C. M. Zhou, D. M. Shi, Y. F. Wang, X. L. Jia, J. Chang, A. Borgna, C. Wang and Y. H. Yang, *Appl. Catal. A-Gen*, 2012, 435, 131-140.

8. Y. Liu, J. Zhou, J. Gong, W. P. Wu, N. Bao, Z. Q. Pan and H. Y. Gu, *Electrochim. Acta*, 2013, 111, 876-887.

9. I. Lee, J. B. Joo, Y. Yin and F. Zaera, *Angew. Chem., Int. Ed.*, 2011, 50, 10208-10211.

10. Y. Liu, B. Liu, Q. Wang, Y. Liu, C. Li, W. Hu, P. Jing, W. Zhao and J. Zhang, *RSC Adv.*, 2014, 4, 5975-5985.

11. S. R. Lingampalli, U. K. Gautam and C. N. R. Rao, *Energ. Environ. Sci.*, 2013, 6,

3589-3594.

12. M. Hino and K. Arata, *Chem. Commun.*, 1999, 53-54.
13. A. A. Madhavan, S. Kalluri, D. K. Chacko, T. A. Arun, S. Nagarajan, K. R. V. Subramanian, A. S. Nair, S. V. Nair and A. Balakrishnan, *RSC Adv.*, 2012, 2, 13032-13037.
14. S. Ameen, M. S. Akhtar, Y. S. Kim and H. S. Shin, *RSC Adv.*, 2012, 2, 4807-4813.
15. H. Li, X. He, Z. Kang, H. Huang, Y. Liu, J. Liu, S. Lian, C. H. Tsang, X. Yang and S. T. Lee, *Angew. Chem. Int. Ed. Engl.*, 2010, 49, 4430-4434.
16. Z. W. Zhang, Y. M. Zhou, Y. W. Zhang, X. L. Sheng, S. J. Zhou and S. M. Xiang, *RSC Adv*, 2014, 4, 40078-40084.
17. X. Chen and S. S. Mao, *Chem. Rev.*, 2007, 107, 2891-2959.
18. Y. Zhang, Y. Zhou, Z. Zhang, S. Xiang, X. Sheng, S. Zhou and F. Wang, *Dalton Trans.*, 2014, 43, 1360-1367.
19. D. D. Lekeufack, A. Brioude, A. Mouti, J. G. Alauzun, P. Stadelmann, A. W. Coleman and P. Miele, *Chem Commun (Camb)*, 2010, 46, 4544-4546.
20. P. Lu, C. T. Campbell and Y. Xia, *Nano Lett.*, 2013, 13, 4957-4962.
21. C. M. Fan, L. F. Zhang, S. S. Wang, D. H. Wang, L. Q. Lu and A. W. Xu, *Nanoscale*, 2012, 4, 6835-6840.
22. M. Cargnello, C. Gentilini, T. Montini, E. Fonda, S. Mehraeen, M. F. Chi, M. Herrera-Collado, N. D. Browning, S. Polizzi, L. Pasquato and P. Fornasiero, *Chem. Mater.*, 2010, 22, 4335-4345.

23. X. Wang, D. Liu, S. Song and H. Zhang, *J. Am. Chem. Soc.*, 2013, 135, 15864-15872.

24. Z. Gu, K. Li, S. Qing, X. Zhu, Y. Wei, Y. Li and H. Wang, *RSC Adv.*, 2014, 4, 47191-47199.

25. J. Qi, J. Chen, G. D. Li, S. X. Li, Y. Gao and Z. Y. Tang, *Energ. Environ. Sci.*, 2012, 5, 8937-8941.

26. D. Bekermann, D. Barreca, A. Gasparotto and C. Maccato, *CrystEngComm*, 2012, 14, 6347-6358.

27. G. Li and Z. Tang, *Nanoscale*, 2014, 6, 3995-4011.

28. X. Zhou, G. Liu, J. Yu and W. Fan, *J. Mater. Chem.*, 2012, 22, 21337-21354.

29. J. J. Liu, S. H. Zou, S. Li, X. F. Liao, Y. J. Hong, L. P. Xiao and J. Fan, *J. Mater. Chem. A*, 2013, 1, 4038-4047.

30. R. L. Spray, K. J. McDonald and K. S. Choi, *J. Phys. Chem. C*, 2011, 115, 3497-3506.

31. A. Umar, M. Abaker, M. Faisal, S. W. Hwang, S. Baskoutas and S. A. Al-Sayari, *J. Nanosci. Nanotechnol.*, 2011, 11, 3474-3480.

32. C. Frandsen, C. R. H. Bahl, B. Lebech, K. Lefmann, L. T. Kuhn, L. Keller, N. H. Andersen, M. von Zimmermann, E. Johnson, S. N. Klausen and S. Morup, *Phys. Rev. B*, 2005, 72.

33. H. Chen, D. Sulejmanovic, T. Moore, D. C. Colvin, B. Qi, O. T. Mefford, J. C. Gore, F. Alexis, S. J. Hwu and J. N. Anker, *Chem. Mater.*, 2014, 26, 2105-2112.

34. C. Hu, X. Zhai, Y. Zhao, K. Bian, J. Zhang, L. Qu, H. Zhang and H. Luo,

Nanoscale, 2014, 6, 2768-2775.

35. L. Guczi, G. Peto, A. Beck, K. Frey, O. Geszti, G. Molnar and C. Daroczi, *J. Am. Chem. Soc.*, 2003, 125, 4332-4337.
36. H. Schmidbaur, *Gold Bull*, 2000, 33, 3-10.
37. Z. W. Zhang, Y. M. Zhou, Y. W. Zhang, S. M. Xiang, S. J. Zhou and X. L. Sheng, *RSC Adv.*, 2014, 4, 7313-7320.
38. Z. Bian, J. Zhu, F. Cao, Y. Lu and H. Li, *Chem Commun (Camb)*, 2009, 3789-3791.
39. Y. Deng, Y. Cai, Z. Sun, J. Liu, C. Liu, J. Wei, W. Li, Y. Wang and D. Zhao, *J. Am. Chem. Soc.*, 2010, 132, 8466-8473.
40. V. Zorba, L. Persano, D. Pisignano, A. Athanassiou, E. Stratakis, R. Cingolani, P. Tzanetakis and C. Fotakis, *Nanotechnology*, 2006, 17, 3234-3238.
41. J. B. Joo, M. Dahl, N. Li, F. Zaera and Y. Yin, *Energy. Environ. Sci.*, 2013, 6, 2082.
42. W. M. Zhang, X. L. Wu, J. S. Hu, Y. G. Guo and L. J. Wan, *Adv. Funct. Mater.*, 2008, 18, 3941-3946.
43. Q. Zhang, D. Q. Lima, I. Lee, F. Zaera, M. Chi and Y. Yin, *Angew. Chem. Int. Ed.*, 2011, 50, 7088-7092.
44. Z. Zhang, Y. Zhou, Y. Zhang, S. Zhou, J. Shi, J. Kong and S. Zhang, *Dalton Trans.*, 2013, 42, 5004-5012.
45. A. Dandapat, A. Mitra, P. K. Gautam and G. De, *Nanomater Nanotechno*, 2013, DOI: 10.5772/56868.

46. L. Sun, W. Wu, S. Yang, J. Zhou, M. Hong, X. Xiao, F. Ren and C. Jiang, *ACS Appl. Mater. Interfaces*, 2013, 6, 1113-1124.

47. M. R. Hasan, S. B. Abd Hamid, W. J. Basirun, Z. Z. Chowdhury, A. E. Kandjani and S. K. Bhargava, *New J. Chem.*, 2015, DOI: 10.1039/C4NJ01048E.

48. D. Channei, B. Inceesungvorn, N. Wetchakun and S. Phanichphant, *Int. J. Photoenergy*, 2013, DOI: 10.1155/2013/484831.

49. Q. Zhang, D. Q. Lima, I. Lee, F. Zaera, M. Chi and Y. Yin, *Angew. Chem., Int. Ed.*, 2011, 50, 7088-7092.

50. Q. Geng and J. Du, *RSC Adv.*, 2014, 4, 16425-16428.

51. X. Wang, D. Liu, S. Song, L. Zeng and Y. Zhang, *Dalton Trans.*, 2012, 41, 7193-7195.

52. R. L. Park, *Science*, 1988, 241, 1839.

53. J. M. Song, S. Y. Chen, Y. L. Shen, C. H. Tsai, S. W. Feng, H. T. Tung and I. G. Chen, *Appl. Surf. Sci.*, 2013, 285, 450-457.

Fig. 1 Schematic illustration for the preparation of the $mSiO_2/Pt/MO_x/Fe$ nanoreactor.

Fig. 2 TEM images of (a) α-Fe_2O_3, (c) $Pt/CeO_2/\alpha$-Fe_2O_3, (d) $Pt/TiO_2/\alpha$-Fe_2O_3, (e) $mSiO_2/Pt/CeO_2/\alpha$-Fe_2O_3, (f) $mSiO_2/Pt/TiO_2/\alpha$-Fe_2O_3. And SEM image of (b) α-Fe_2O_3.

Fig. 3 UV-Vis diffuse reflectance spectra of (a) TiO_2/α-Fe_2O_3, (b) $Pt/TiO_2/\alpha$-Fe_2O_3, (c) $mSiO_2/Pt/TiO_2/\alpha$-Fe_2O_3. All the particles were dispersed in ethanol solution.

Fig. 4 (a) A highresolution TEM image of the loaded CeO_2 NPs; (b) The SAED pattern obtained from $Pt/CeO_2/\alpha$-Fe_2O_3 sample; (c,d) The EDX analysis of $Pt/CeO_2/\alpha$-Fe_2O_3 sample and $Pt/TiO_2/\alpha$-Fe_2O_3 sample respectively; and (e,f) TEM images of the obtained $mSiO_2/Pt/CeO_2/Fe$ sample and $mSiO_2/Pt/TiO_2/Fe$ sample, the two samples were calcined at 500 °C.

Fig. 5 XRD patterns of (a) $mSiO_2/Pt/CeO_2/\alpha$-Fe_2O_3, (b) $Pt/TiO_2/\alpha$-Fe_2O_3, (c) $mSiO_2/Pt/CeO_2/Fe$, (d) $mSiO_2/Pt/TiO_2/Fe$. All the samples were calcined at 500 °C.

Fig. 6 (a) Successive UV-vis adsorption spectra of the reduction of 4-NP by $NaBH_4$ in the presence of $mSiO_2/Pt/TiO_2/Fe$ catalyst calcined at 500 °C; (b) Plots of $\ln(C_o/C_t)$ of 4-NP against time: (1,4) calcined $mSiO_2/Pt/CeO_2/Fe$ at 500 °C (Ce-500) and 700 °C (Ce-700) respectively, (2,3) calcined $mSiO_2/Pt/TiO_2/Fe$ at 500 °C (Ti-500) and 700 °C (Ti-700) respectively; (c,d) Comparison of the Pt NP size of the Ti-500 and Ti-700. The insets in each image were the Pt NP size

distribution histograms; (e,f) TEM images of Ce-500 and Ce-700 respectively.

Fig. 7 Speculated mechanism of the catalytic reduction of 4-NP with the $mSiO_2/Pt/MO_x/Fe$ catalyst.

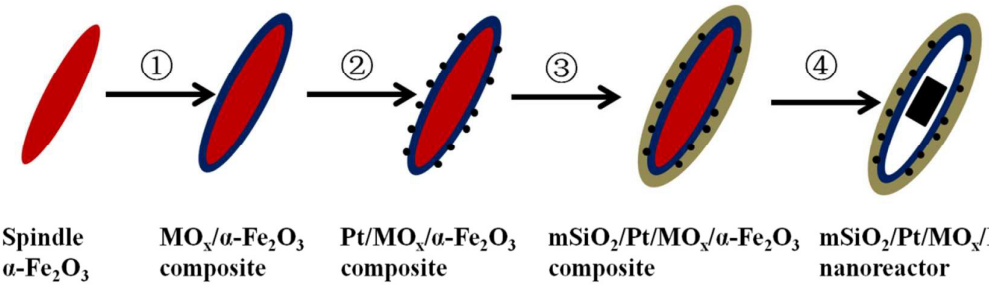

Fig. 1 Schematic illustration for the preparation of the $mSiO_2/Pt/MO_x/Fe$ nanoreactor.

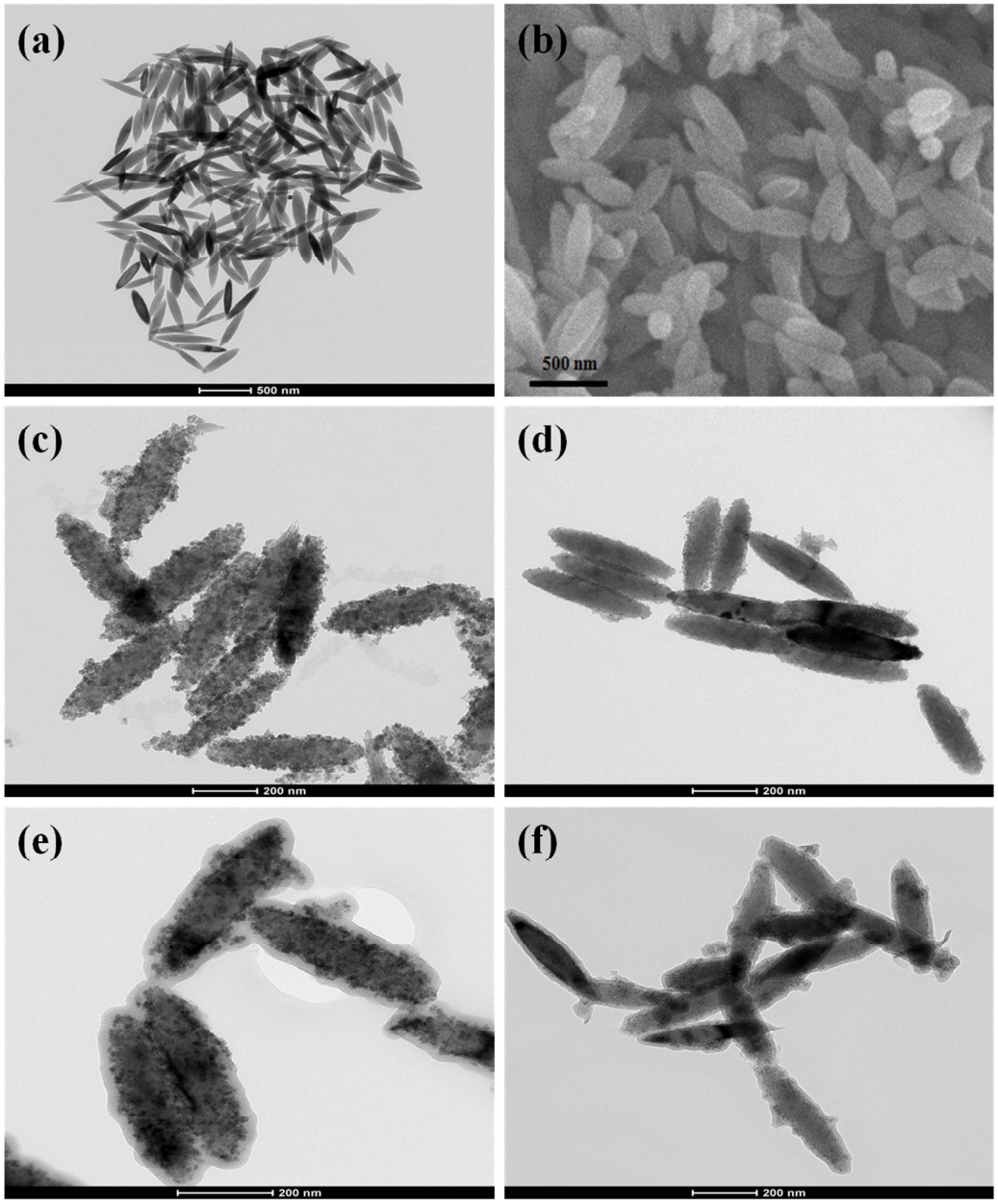

Fig. 2 TEM images of (a) α-Fe_2O_3, (c) Pt/CeO_2/α-Fe_2O_3, (d) Pt/TiO_2/α-Fe_2O_3, (e) mSiO_2/Pt/CeO_2/α-Fe_2O_3, (f) mSiO_2/Pt/TiO_2/α-Fe_2O_3. And SEM image of (b) α-Fe_2O_3.

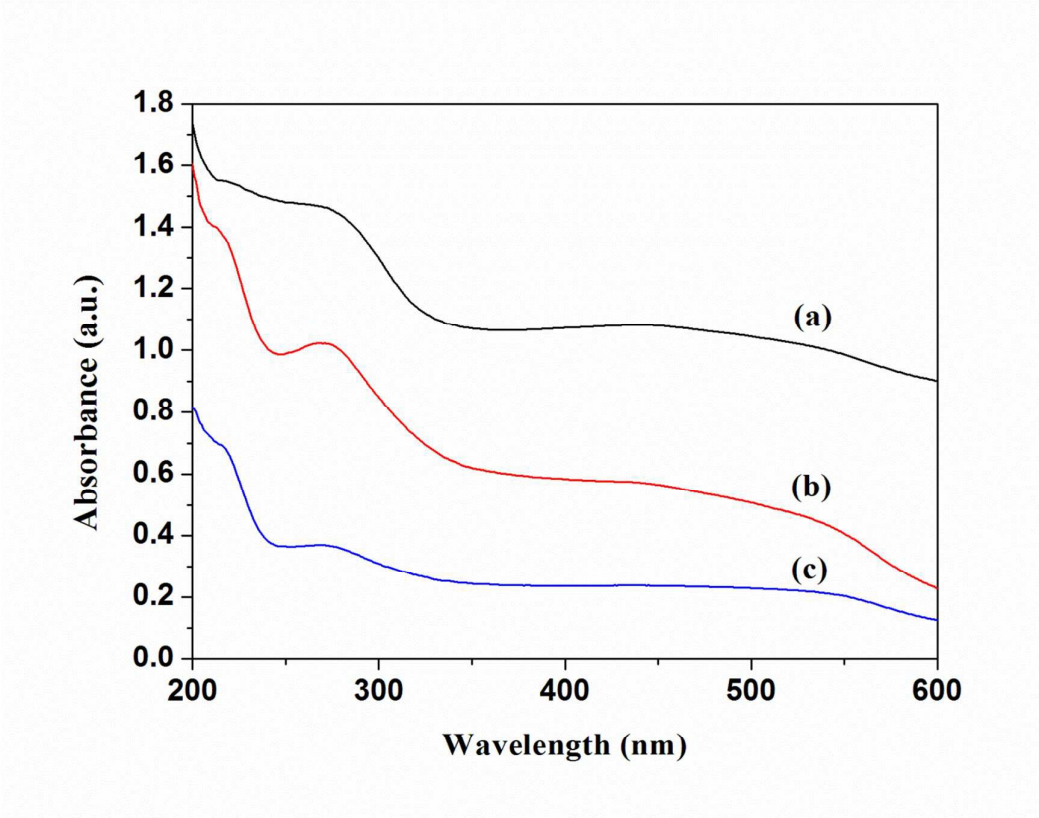

Fig. 3 UV-Vis diffuse reflectance spectra of (a) TiO_2/α-Fe_2O_3, (b) Pt/TiO_2/α-Fe_2O_3, (c) mSiO_2/Pt/TiO_2/α-Fe_2O_3. All the particles were dispersed in ethanol solution.

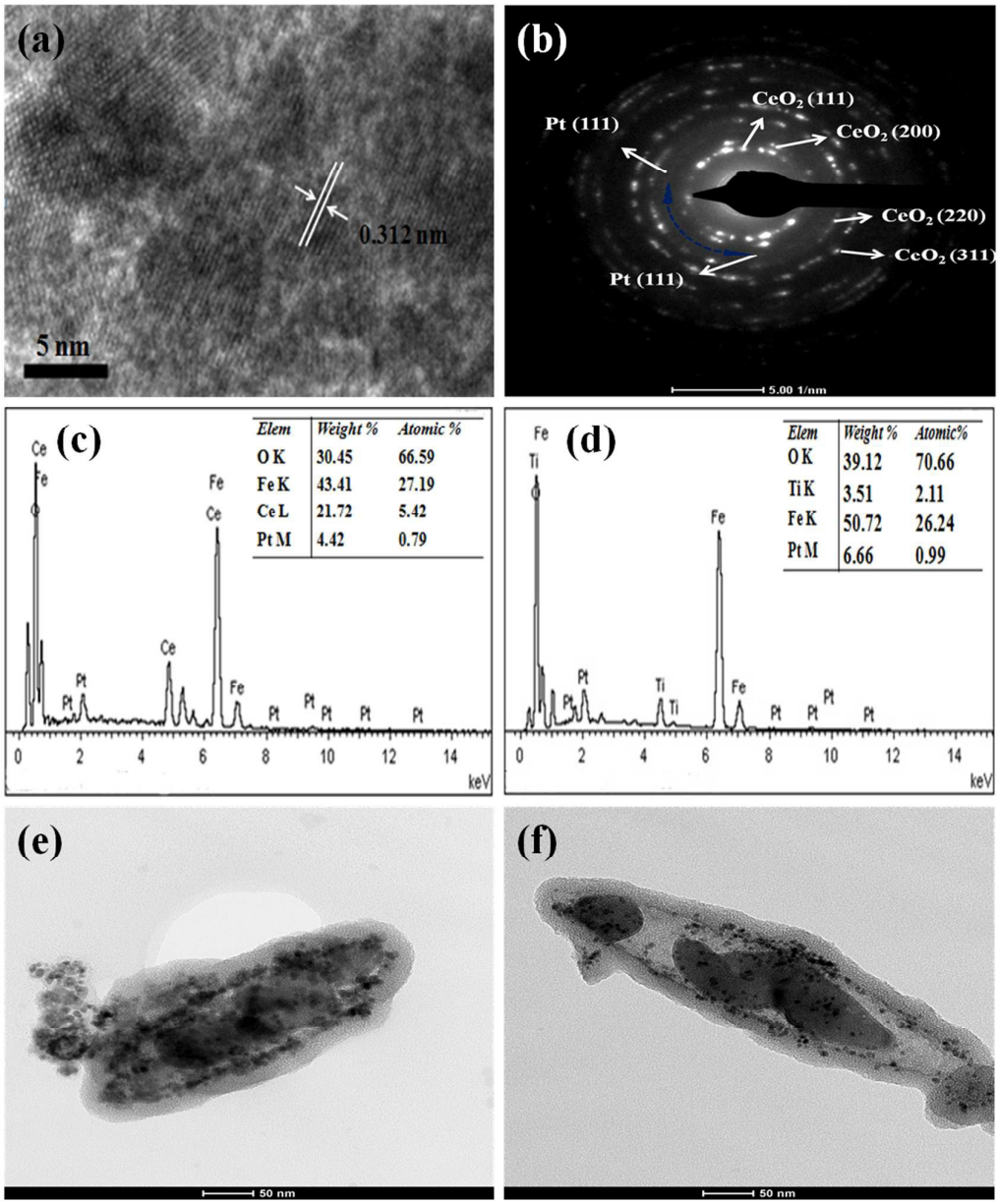

Fig. 4 (a) A highresolution TEM image of the loaded CeO_2 NPs; (b) The SAED pattern obtained from Pt/CeO_2/α-Fe_2O_3 sample; (c,d) The EDX analysis of Pt/CeO_2/α-Fe_2O_3 sample and Pt/TiO_2/α-Fe_2O_3 sample respectively; and (e,f) TEM images of the obtained mSiO_2/Pt/CeO_2/Fe sample and mSiO_2/Pt/TiO_2/Fe sample, the two samples were calcined at 500 °C.

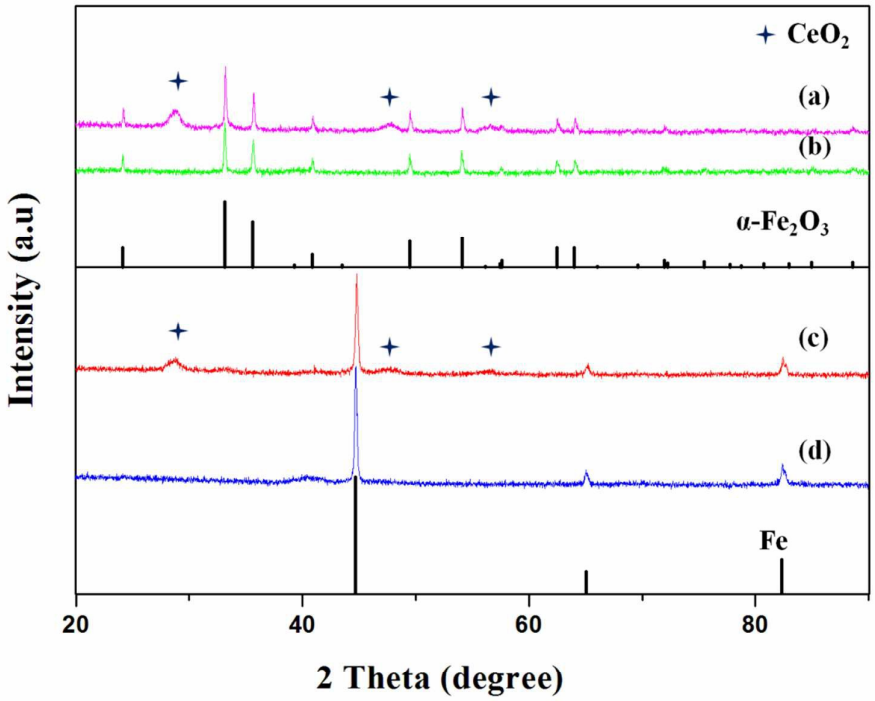

Fig. 5 XRD patterns of (a) $mSiO_2/Pt/CeO_2/\alpha\text{-}Fe_2O_3$, (b) $Pt/TiO_2/\alpha\text{-}Fe_2O_3$, (c) $mSiO_2/Pt/CeO_2/Fe$, (d) $mSiO_2/Pt/TiO_2/Fe$. All the samples were calcined at 500 °C.

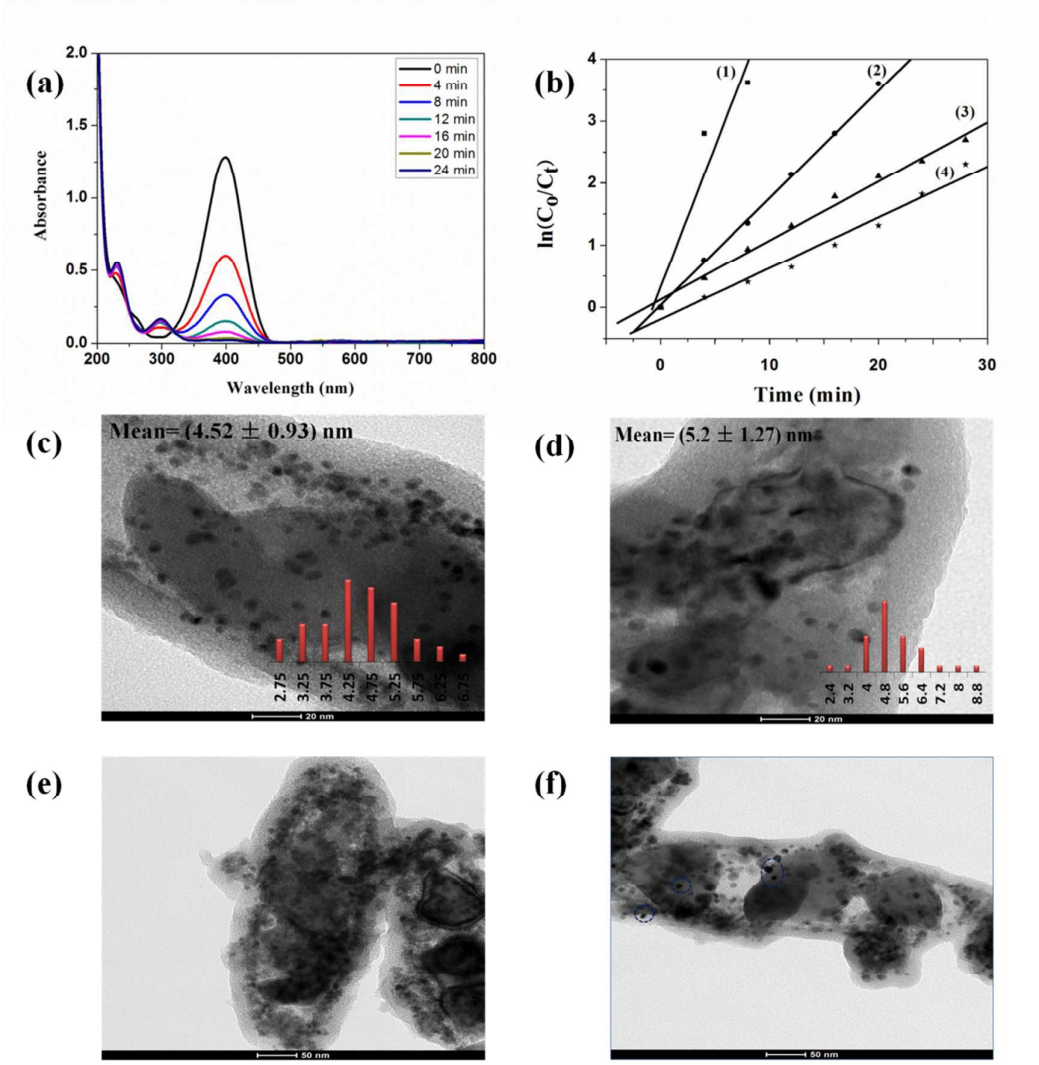

Fig. 6 (a) Successive UV-vis adsorption spectra of the reduction of 4-NP by $NaBH_4$ in the presence of $mSiO_2/Pt/TiO_2/Fe$ catalyst calcined at 500 °C; (b) Plots of $\ln(C_o/C_t)$ of 4-NP against time: (1,4) calcined $mSiO_2/Pt/CeO_2/Fe$ at 500 °C (Ce-500) and 700 °C (Ce-700) respectively, (2,3) calcined $mSiO_2/Pt/TiO_2/Fe$ at 500 °C (Ti-500) and 700 °C (Ti-700) respectively; (c,d) Comparison of the Pt NP size of the Ti-500 and Ti-700. The insets in each image were the Pt NP size distribution histograms; (e,f) TEM images of Ce-500 and Ce-700 respectively.

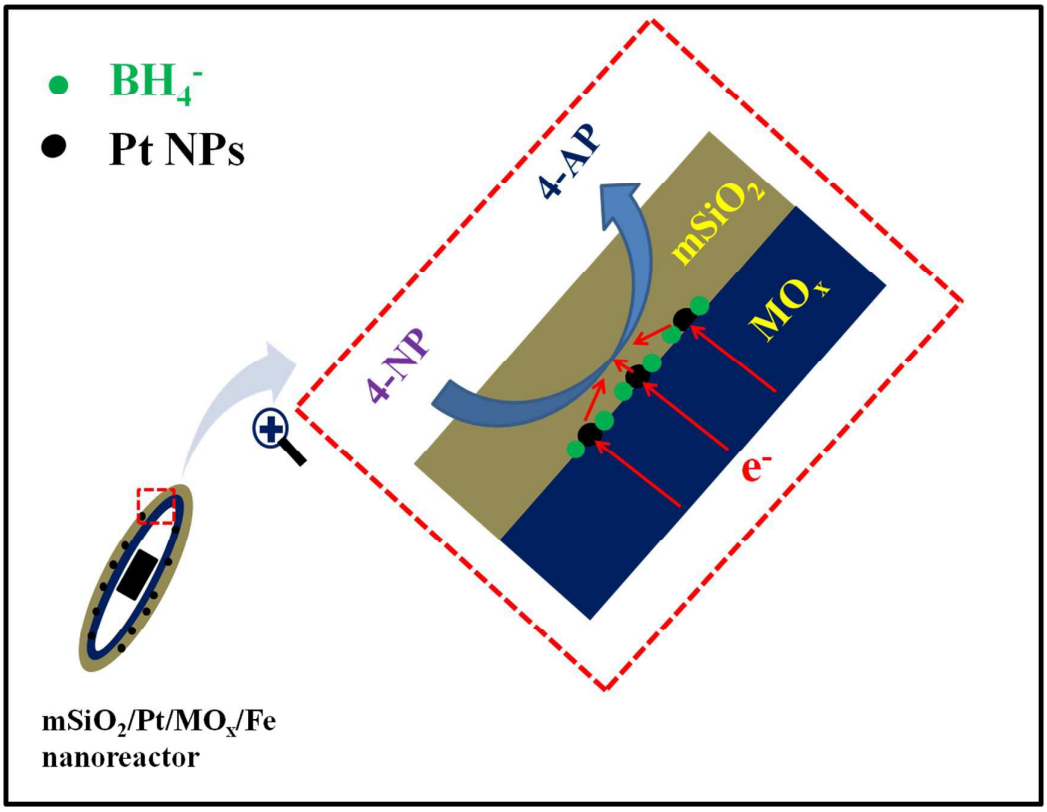

Fig. 7 Speculated mechanism of the catalytic reduction of 4-NP with the $mSiO_2/Pt/MO_x/Fe$ catalyst.